JOURNAL OF GEOPHYSICAL RESEARCH, VOL. 102, NO. D22, PAGES 26,301–26,313, NOVEMBER 27, 1997

Observational evidence of wave ducting and evanescence in the mesosphere

Joseph R. Isler[1]
Laboratory for Atmospheric and Space Physics, University of Colorado, Boulder

Michael J. Taylor
Space Dynamics Laboratory and Physics Department, Utah State University, Logan

David C. Fritts
Colorado Research Associates, Boulder

Abstract. A collaborative radar and imaging study of gravity waves over the Hawaiian Islands was performed during October 1993 as part of the Airborne Lidar and Observations of Hawaiian Airglow 1993/Coupling and Dynamics of Regions Equatorial (ALOHA-93/CADRE) campaign to investigate the propagation characteristics of short-period (<1 hour) waves at nightglow altitudes. The horizontal wavelengths and apparent phase speeds of quasi-monochromatic wave events were measured in four separate nightglow emissions using data obtained by a high-resolution CCD imager. This information was correlated with simultaneous MF radar wind measurements over the same height interval (~80–100 km) to infer intrinsic wave parameters in each case. Correlating the two data sets allowed the determination of the local vertical wavenumber for each event, in particular whether it be real (indicative of freely propagating waves) or imaginary (indicative of ducted or evanescent waves). The results of this study indicate a preponderance of ducted or evanescent waves at 80–100 km during the time of the observations, with up to ~75% of the events recorded exhibiting ducted or evanescent behavior. Also noted was a tendency for ducted behavior to be more prevalent among waves with shorter horizontal wavelengths, in agreement with Doppler ducting theory. These results suggest that ducted waves are relatively common in the upper mesosphere and lower thermosphere region, at least over the mid-Pacific Ocean. As small-scale waves which are ducted have the potential to travel much longer horizontal distances than freely propagating waves, the frequency of their occurrence should be taken into account in efforts to quantify gravity wave effects at these altitudes.

1. Introduction

Previous optical and radar studies have revealed a wealth and diversity of waves in the middle and upper atmosphere. Resonant sodium lidars, for example, have proven to be most responsive to wave motions with vertical wavelengths less than the depth of the sodium layer (~10 km). For periodicities >1 hour, which are often reported, the small vertical wavelengths imply waves with horizontal scales of $\sim 10^2$–10^3 km. The distinct downward phase progression that often accompanies these wave-like variations provides strong evidence that they are due to freely propagating internal gravity waves of lower atmospheric origin. In comparison, image measurements of the nightglow emissions (primarily image measurements of the near-infrared (NIR) OH emission at ~87 km and $O_2(0,1)$ emission layers) have demonstrated a high sensitivity to smaller horizontal scale (<100 km), shorter-period (<1 hour) waves [e.g., *Taylor and Hill*, 1991; *Hecht et al.*, 1994; *Swenson et al.*, 1995]. Such nightglow observations typically involve line-of-sight summation over an entire vertical (possibly oblique) viewing column, yielding information on horizontal wave parameters only. For this reason, when observations involve only a single emission layer, information on the vertical wave parameters can only be inferred using the horizontal wave parameters and the gravity wave dispersion relationship [*Hines*, 1960]. However, without a knowledge of the background winds (which allows determination of intrinsic wave parameters), this technique entails large uncertainties in the inferred vertical wavelengths. As a consequence, most previous investigations of small-scale gravity waves have simply assumed that the wave motions were of a freely propagating nature. In this paper we describe a new capability for investigating the propagation characteristics of these waves. The method utilizes image measurements from four nightglow emission layers (spanning the height range ~80–100 km) which when combined with simultaneous wind measurements provides a powerful technique for assessing the true propagation characteristics of the wave motions.

While there has been considerable theoretical research on wave ducting mechanisms in the upper atmosphere [*Francis*, 1974; *Tuan and Tadic*, 1982; *Chimonas and Hines*, 1986; *Wang and Tuan*, 1988; *Fritts and Yuan*, 1989], the interpretation of

[1]Now at Physics Department, Wagner College, Staten Island, New York.

Copyright 1997 by the American Geophysical Union.

Paper number 97JD01783.
0148-0227/97/97JD-01783$09.00

Table 1. Summary of Filter Characteristics and Operational Parameters

Filter[a]	Emission, nm	Assumed Height, km	Bandwidth, nm	Transmission, %	Exposure Time, s
1	OI (557.7)	96	2.67	81	90
2	$O_2(0, 1)$	94	12.0	85	90
3	NIR OH[b]	87	715–930	87	20
4	Na (589.2)	90	2–37	81	120
5	Bg (572.5)	···	2–65	83	90

[a]Filter sequence 1, 5, 4, 1, 3, 2.
[b]With a 20-nm notch at 865 nm to suppress the $O_2(0, 1)$ emission.

wave spectra and the inferences for wave fluxes based upon available observational data have usually assumed freely propagating waves [e.g., *Smith et al.*, 1987]. This assumption is particularly critical for small-scale waves for the following reasons: (1) freely propagating small-scale waves have been shown to be the most important waves contributing to wave mean flow forcing and momentum deposition in the mesosphere and lower thermosphere [*Fritts*, 1984], and (2) small-scale waves are highly susceptible to thermal and Doppler ducting in the mesopause region and hence they can travel considerable distances horizontally before contributing irreversible changes to the environment.

Optical measurements of the nightglow emissions provide an important tool for determining the occurrence and horizontal characteristics of small-scale, short-period waves at the emission altitudes [*Taylor et al.*, 1987; *Taylor and Hapgood*, 1990]. While the measured horizontal wavelength is an intrinsic parameter, the measured phase speed (and hence the observed wave period) may differ significantly from the intrinsic phase speed (and intrinsic wave period) due to the presence of background winds. However, when multilayer nightglow data are combined with simultaneous wind measurements, intrinsic wave parameters can be investigated over a range of heights, permitting an in-depth study of the propagation characteristics of the wave motions and a more precise comparison with theoretical predictions. In particular, these can help to quantify the importance of small-scale wave ducting in the mesosphere and lower thermosphere for the first time. In this paper, we use novel all-sky imaging data and radar wind data obtained during the Airborne Lidar and Observations of Hawaiian Airglow 1993/Coupling and Dynamics of Regions Equatorial (ALOHA-93/CADRE) campaign to assess the characteristics and frequency of occurrence of ducted versus freely propagating small-scale wave motions over the mid-Pacific Ocean. Joint measurements were made over the new moon period October 6–22, 1993.

2. Measurement Techniques and Data Analysis

2.1. Imaging Gravity Waves

The imaging data involved optical observations of four nightglow emissions using a large field (180°), monochromatic imaging system located at the Department of Energy DOE building near the summit (2970 m) of Haleakala Crater, Maui (156°W, 21°N). The imager was designed to investigate gravity wave structures over the 80–100 km range by sequentially recording wave signatures in four nightglow emissions: the NIR OH and O_2 band emissions and the OI (557.7 nm) and Na (589.2 nm) line emissions. A brief description of the system is given by *Taylor et al.* [1995a]. The camera consists of a thermoelectrically cooled, bare (1024 × 1024 pixel), charge-coupled device (CCD) of high quantum efficiency, ~80% at visible and ~50% at NIR wavelengths. The large dynamic range and low noise characteristics of this device (dark current $<0.5\ e\ \text{pixel}^{-1}\ \text{s}^{-1}$) provide an exceptional capability for quantitative measurements of faint, low contrast (<5%) gravity waves. The imager was fitted with a fast (f/4) all-sky (180°) telecentric lens system and a temperature stabilized filter wheel. The OH measurements were made using a broad band filter of bandwidth 715–930 nm incorporating a notch at ~865 nm to suppress contributions from the $O_2(0, 1)$ band. The $O_2(0, 1)$ band was isolated using a 12-nm bandwidth filter centered at 865.5 nm. Each line emission was selected using high transmission (typically 60–80%) interference filters of ~2.5 nm half bandwidth. In addition to these observations a background sky measurement was made at 572.5 nm (half width 2.7 nm) to aid the interpretation of the visible wavelength data. Integration times determined for these measurements ranged from 15 s for the bright OH emission to 90 s for the OI (557.7 nm) and O_2 emissions and 120 s for the faint NaD lines. A summary of the filter characteristics and operational parameters for this campaign is given in Table 1. Sequential measurements were made every ~9 min except for the OI (557.7 nm) emission which was sampled twice per cycle.

Quasi-monochromatic events in the all-sky data were identified, and their times of occurrence were noted. These events were then measured to determine the horizontal parameters of the wave motions: horizontal wavelengths, phase speeds, and directions of motion. The images were calibrated first using the star background to determine the elevation and azimuth of any point in the image field. (The typical accuracy of this calibration is to within 1 pixel, equivalent to ~20 arc min.) A description of this procedure, as applied to narrow angle data, is given by *Hapgood and Taylor* [1982]. To correct for geometrical distortion arising from nonparallel lines of sight in the image itself, the outline of prominent wave crests in each image was traced and mapped onto the ground, assuming a centroid emission altitude of 87 km for the OH emission [*Baker and Stair*, 1988], 90 km for the Na emission [*Greer and Best*, 1967], and 94 km for the O_2 and 96 km for the OI (557.7 nm) emissions [*Offermann and Drescher*, 1973]. For each wave event, measurements from a time series of images and maps were used to determine the mean horizontal wavelength, observed phase speed, and predominant direction of motion (usually determined to within an accuracy of ±5°). On some occasions the direction of motion was observed to rotate by as much as ~20–30° over a period of several hours and with altitude. In these cases we have used the wave direction at the central time of observation for the intrinsic wave calculations.

The nominal full width at half maximum (FWHM) of the emission layers (~5–10 km) and the horizontal field of view of the all-sky imager at nightglow altitudes (~500 km radius) provide natural limits for these measurements. Because of destructive interference within the layer for smaller-scale motions, the FWHM of an emission layer sets an approximate lower limit to the vertical wavelengths of the motions that can be detected. Similarly, the horizontal field of view sets an upper limit of ~250 km on the horizontal wavelengths to which the imaging technique is sensitive [*Taylor et al.*, 1995c]. (Larger-scale waves have been detected using a time series of image measurements, but their two-dimensional morphology is not easily determined.) However, as will be shown later, all of the

waves imaged during this campaign exhibited significantly shorter horizontal wavelengths.

2.2. MF Radar Winds

The wind data used for this study were collected by a medium frequency (MF) radar system located at the Pacific Missile Range Facility (PMRF) at Barking Sands, Kauai, Hawaii (160°E, 22°N). The mode of operation and data processing algorithms for this system are described in detail by *Fritts and Isler* [1994]. Nominal wind estimates were obtained at 2-min intervals and 2-km vertical spacing from 60 to 100 km during daytime and from 70 to 100 km during nighttime. As nighttime data tend to be somewhat sparse below 82 km, and since the airglow imager only operated at nighttime, the effective altitude range of the radar for this study is ~82–98 km.

The MF wind data were used to approximate the mean wind environment over Maui, where the CCD imager was located, ~375 km to the southeast of Kauai (Figure 1). Because of the spatial separation of the ground stations, temporal averages of the winds over Kauai were used to represent mean winds over Maui. We have used 3-hour averages of the winds over Kauai for this purpose. Since Doppler ducts arise due to structures in the lower-frequency winds which trap higher-frequency wave motions (see section 3), an estimate of the horizontal scale of a Doppler duct can be made by assuming it to be due to a motion with a period ~6 hours or longer. From the gravity wave dispersion relationship one can infer that motions with periods greater than 6 hours will have a ratio of horizontal to vertical scales of greater than 60 to one. Thus waves with vertical scales representative of typical wind variations (≥10 km) will have horizontal scales ≥600 km, so using 3-hour mean winds should provide sensitivity to ducts that have a horizontal extent comparable to or larger than the distance between the ground stations.

3. Wave Ducting Theory

Linear gravity wave theory was first developed for the simplified but illustrative case of an atmosphere which is stratified in density and pressure but assumed to be windless, isothermal, irrotational, and inviscid. The resulting governing equations were shown to admit traveling acoustic and gravity wave solutions [*Hines*, 1960]. The dispersion characteristics and intrinsic properties of these waves, as well as their observed amplitudes and scales, led to the first understanding of their importance for momentum and energy transports, particularly in the upper atmosphere (see *Fritts* [1984] for a review of the historical development). Given that the atmosphere has a variable thermal profile, ubiquitous mean winds, and increasing kinematic viscosity with altitude, it was natural that the theory would be advanced further by the relaxation of the simplifying constraints imposed on the background atmosphere. For our purpose here, we note that for wave propagation in general in any medium, inhomogeneities in the medium will give rise to wave refraction and possible wave reflection. In the atmosphere, the inhomogeneities of importance to gravity wave propagation are gradients in background temperature (or more precisely in the stability) and in the wind field. When such gradients give rise to wave reflection, wave ducts (or waveguides, as they are sometimes called) may also occur. The importance of these wave ducts in the atmosphere arises from the fact that waves trapped in well-defined ducts can propagate large horizontal distances with little attenuation.

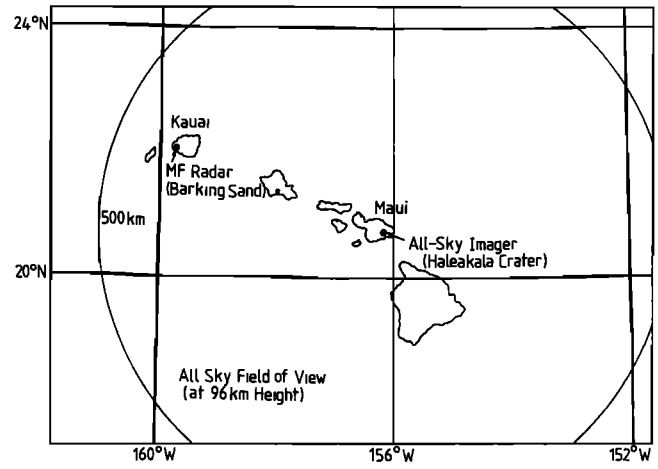

Figure 1. Map of observing geometry. Note the field of view of the all-sky camera encompasses the Kauai MF radar site at a range of 375 km.

A good starting point from which to understand wave ducting mechanisms comes from an examination of the Taylor-Goldstein equation, which is the second-order linear, inviscid equation for the vertical velocity field. The Taylor-Goldstein equation can be derived from the linear, inviscid equations of motion after neglecting compressibility effects (acoustic motions) and assuming solutions periodic in time and in the horizontal direction. The Taylor-Goldstein equation is

$$w'_{zz} + \left[\frac{N^2}{(\bar{u}-c)^2} - \frac{\bar{u}_{zz}}{(\bar{u}-c)} - k^2\right] w' = 0 \qquad (1)$$

where the subscripts denote partial derivatives, w' is the vertical velocity, N is the buoyancy frequency, $\bar{u}$ is the horizontal wind in the direction of wave propagation, and c and k are the horizontal phase speed and wavenumber, respectively. The most general form of this equation contains additional shear and constant terms associated with compressibility effects; we have neglected these terms because in all the cases studied, the wave phase speeds were much less than the speed of sound. To validate our use of the simplified expression (1), we included the terms associated with compressibility and found our results to be no different than when those terms were neglected.

In equation (1), both N and $\bar{u}$ are functions of altitude. If these are slowly varying functions, WKB solutions can be obtained. Of course, for very narrow velocity jets or steep shears (i.e., $\bar{u}$ varying rapidly), the use of WKB solutions may not be justified. The wind profiles used in this study did not exhibit such rapid variations in $\bar{u}$, though in some cases the WKB approximation may be only marginally justified. However, in order to make quantitative use of Doppler ducting theory, we take WKB solutions to equation (1), with vertical wavenumber m given approximately by

$$m^2 \approx \frac{N^2}{(\bar{u}-c)^2} - \frac{\bar{u}_{zz}}{(\bar{u}-c)} - k^2 \qquad (2)$$

It is now easy to see how wave reflection occurs: if N^2 or $\bar{u}$ or both together vary with altitude so as to make $m^2 < 0$, a region of evanescence exists in which the wave cannot freely propagate, causing reflection of wave energy.

Earlier work focused on wave ducting due to mean temperature gradients in the atmosphere and deliberately assumed a

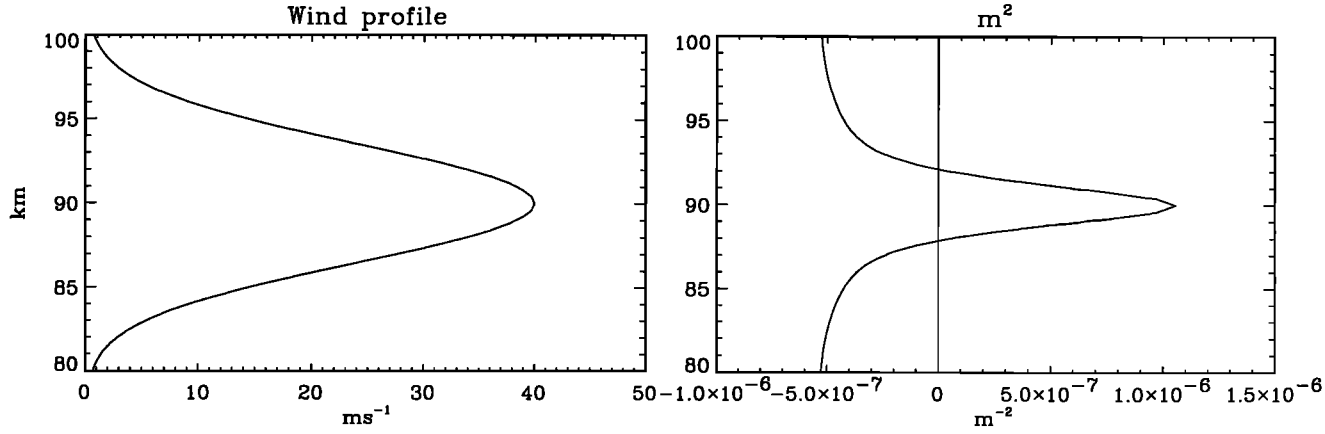

Figure 2. Sketch of a theoretical Doppler duct due to mean wind fields.

zero mean wind. The ducts due to temperature gradients are called thermal ducts, and a good summary of their dominant wave modes is given by *Francis* [1974]. These are relatively stable, long-lived ducts, which tend to support waves with high horizontal phase speeds and large vertical scales. However, it is smaller-scale waves which play the more important role in wave-mean flow interactions, because of their larger fluxes of wave energy and momentum [*Fritts*, 1989]. Because these motions are typically slower, it is essential to account for wind variations in describing their responses to varying atmospheric conditions.

A theory of wave ducting due to variation in the mean wind has been formulated [*Chimonas and Hines*, 1986]. These ducts are called Doppler ducts. As mean winds are highly variable both spatially and temporally, they give rise to ducted modes having a wide range of phase speeds and vertical scales. Thus, although they may be shorter-lived than thermal ducts, Doppler ducts are potentially more important for the atmospheric circulation because of their potential to trap smaller-scale waves. Such smaller-scale, guided waves could then travel large horizontal distances before their transports of energy and momentum interact with the mean flow.

Theoretically, Doppler ducts can occur whenever the mean wind profile has a local maximum (or minimum) slightly less (or more) than the observed wave phase speed. The increase of $(\bar{u} - c)^2$ away from the local wind maximum or minimum can lead to regions of evanescence on either side of a region of vertical propagation (see equation (2)). To illustrate this situation, a sketch of an idealized Doppler duct is presented in Figure 2.

In the present study we consider only the effects of Doppler ducting. For this purpose, we have evaluated m^2 in equation (2) using the airglow observations to provide estimates of c and k and the Hawaii radar data to provide estimates of $\bar{u}$ and have taken N^2 to be constant (0.0002 s^{-2}). Considering only the effects of Doppler ducting should not be too severe a restriction since the observations reported here occurred near the winter mesopause, where N^2 is slowly varying in the mean. For lower-frequency motions which might give rise to Doppler ducts, N^2 is more variable, but as will be seen, $\bar{u}$ was highly variable over this region, and variations in $\bar{u}$ appear quadratically in equation (2), so it is expected that variations in $\bar{u}$ would be more important than variations in N^2. In any case, we have no choice but to take N^2 to be constant, as coincident temperature measurements were not made.

Since the observations reported here occurred over a limited altitude range, as will be seen, it was not always possible to identify both edges of a suspected Doppler duct.

Finally, we note that in the following analysis we have evaluated the second term on the right-hand side of equation (2) numerically using a three-point algorithm applied to the radar data. Sensitivity tests showed that this term could not simply be neglected. For example, consider the case of a Doppler duct associated with a velocity jet. Near the jet maximum, $\bar{u}_{zz}$ is negative, so that the second term in (2) is negative (since $c > \bar{u}$), while near the edge of the jet, $\bar{u}_{zz}$ is positive, so that the second term in (2) positive. Thus the overall effect of this term is to decrease m^2 in the center of the duct and to increase m^2 near the edge of the duct. However, there is unavoidable uncertainty in evaluating a second derivative numerically from a wind profile with nine or fewer data points. So we have evaluated m^2 both with and without the curvature term and compared the results for each event. In all of the cases studied, its effect was negligible or in the case of a ducted motion its effect was to lower the value of m^2 inside the duct, and somewhat broaden the width of the duct, but not to fundamentally alter its character. In the results which follow, the curvature term has been included.

4. Results and Discussion

4.1. Analysis of the Images

Table 2 lists the results of an ensemble of wave measurements using the CCD image data during the ALOHA-93 campaign. These results represent a significant fraction of the total data set analyzed to date. For convenience, we have listed the events in chronological order and have assigned each event a number to simplify its identification. Table 2 lists the day of year and mean time (UT) of observation for each wave event, the emissions in which the wave event was most readily observed, the observed phase speed c, the mean wind in the direction of wave propagation $\bar{u}$ as measured by the MF radar, and the horizontal wavelength λ_h. (The rest of Table 2 is described in section 4.2.) Several events exhibited exceptionally clear wave structure in some but not all of the nightglow emissions: for example, events 2, 11, 15, 22, and 33. In comparison, some events, such as events 10, 13, 26, and 36, were prominent in all four nightglow emissions. One of these, event 13, exhibited an unusual reversal in contrast between the OH and OI structures and has already been reported on elsewhere

Table 2. Gravity Wave Events Used for This Study, With Corresponding Wave Parameters as Determined, or Inferred, From the Image and Radar Data

Wave Event	Day of Year	Time, UT	Emission	c	$\bar{u}$	λ_h	λ_z	Propagating	Ducted	Evanescent	Evanescent or Ducted
1	280	1045	OI, Na, OH	37	9	20	10–50	X			
2	281	0720	OI	58	−8	16			X		
3	281	0900	OI, O_2, Na, OH	42	−15	36	15–50	X			
4	281	1030	OI, Na, OH	34	2	21	12–30	X			
5	282	0700	OI, O_2, Na	69	15	12				X	
6	282	1025	OI	60	−12	27					X
7	282	1030	OI, O_2, Na, OH	54	10	25					X
8	282	1110	OI, O_2, Na, OH	61	9	10				X	
9	282	1240	OI, O_2, Na, OH	54	−9	22				X	
10	282	1330	OI, O_2, Na, OH	39	−13	23				X	
11	283	0930	OI, Na	48	28	13					X
12	283	0940	OI, O_2, Na, OH	38	0	19			X		
13	283	1100	OI, O_2, Na, OH	76	−15	19				X	
14	283	1100	OI, O_2	56	9	16				X	
15	284	1240	OI, O_2	36	−23	19				X	
16	285	1410	OI, O_2, Na	41	−55	27				X	
17	286	1200	OI, O_2, Na, OH	60	−21	32				X	
18	286	1330	OI, O_2, Na, OH	50	30	18					X
19	286	1330	OI, O_2, Na	89	−24	17				X	
20	286	1411	OI, O_2, Na	70	−35	12				X	
21	286	1500	OI, O_2, Na	61	20	14			X		
22	287	1100	OI, O_2	61	18	30			X		
23	288	0950	OI, O_2, Na	76	9	53					X
24	291	0730	OI, O_2, Na, OH	59	−11	16				X	
25	291	1400	OI, O_2, Na, OH	35	11	14					X
26	292	0930	OI, O_2, Na, OH	57	24	14					X
27	292	1235	OI, Na, OH	97	−8	19				X	
28	292	1430	OI, O_2, Na, OH	45	15	15			X		
29	293	1030	OI, O_2, Na, OH	39	6	21	10–20	X			
30	293	1325	OI, O_2	50	0	29	40–80	X			
31	293	1340	OI, O_2, Na, OH	37	−22	20					X
32	293	1350	OI, O_2, Na, OH	38	−11	22					X
33	294	1140	OI, O_2	33	8	20	7–14	X			
34	294	1310	OI, O_2, Na, OH	53	−3	30	10–40	X			
35	295	0930	OI, O_2, Na, OH	40	−24	19					X
36	295	1230	OI, O_2, Na, OH	34	−20	38	15–55	X			

Units for velocities are m s^{-1}; units for wavelengths are km.

[*Taylor et al.*, 1995b]. Table 2 shows that on average only about 50% of the wave events were detected in all four nightglow emissions. In general, the OI emission provided images with the greatest contrast, followed by OH, O_2, and Na, in that order. The wave structure was usually most prominent in one or two emissions (e.g., OH and Na or OI and O_2) and of significantly lower contrast (or absent) in the other emissions. This fact suggests that Doppler ducting may have played an important role during this campaign, but by itself does not provide evidence to that effect, since other processes such as wave breaking or critical level encounters could easily account for localized altitude responses as well.

Figure 3 shows an example of wave structure imaged in all four emissions. This display, event 26, was observed on October 19 and its progression over the Hawaiian Islands was also recorded by a second imager located on Mauna Loa, Hawaii [*Swenson et al.*, 1995], ~450 km to the southeast of Maui (see Figure 1). This display was unusual in that it exhibited a limited number of wave crests (three to four) that moved rapidly southward at ~60 m s^{-1}, indicating a wave period of ~5 min, close to the local buoyancy period. The leading edge and the following wave crests are easily identifiable in each emission permitting a good estimation of the relative positions of the phase fronts (discussed later) and have yielded an accurate measurement of the wave structure in the OI emission indicating a mean height of 95 ± 2 km [*Taylor et al.*, 1995d]. As this pattern was evident in all four emissions extending over the height range ~80–100 km, it may be expected that it is the signature of a freely propagating wave. However, the MF radar data (presented in section 4.2) suggest that it was evanescent in nature. Further evidence in support of this result is given later (Figure 7) when the phase relationship of these waves are examined for different emission altitudes.

Examples of wave data recorded on other nights during the campaign are shown in Figure 4, corresponding to events 2, 10, 13, 25, 24, and 36 (Figure 4a–4f). Prominent wave structures are obvious features of each of these images, representing a variety of wave motions. As will be seen, the waves shown here were inferred to have a range of propagation characteristics, from ducted or evanescent to freely propagating. However, as can be seen, no obvious characteristics of the individual images were found to distinguish ducted or evanescent waves from freely propagating waves.

When images of the same waveforms are clearly identifiable in data from more than one emission, it is possible to estimate whether or not the waves are vertically propagating, since the four nightglow emissions are centered at separate heights. The images from different emissions were made at slightly different

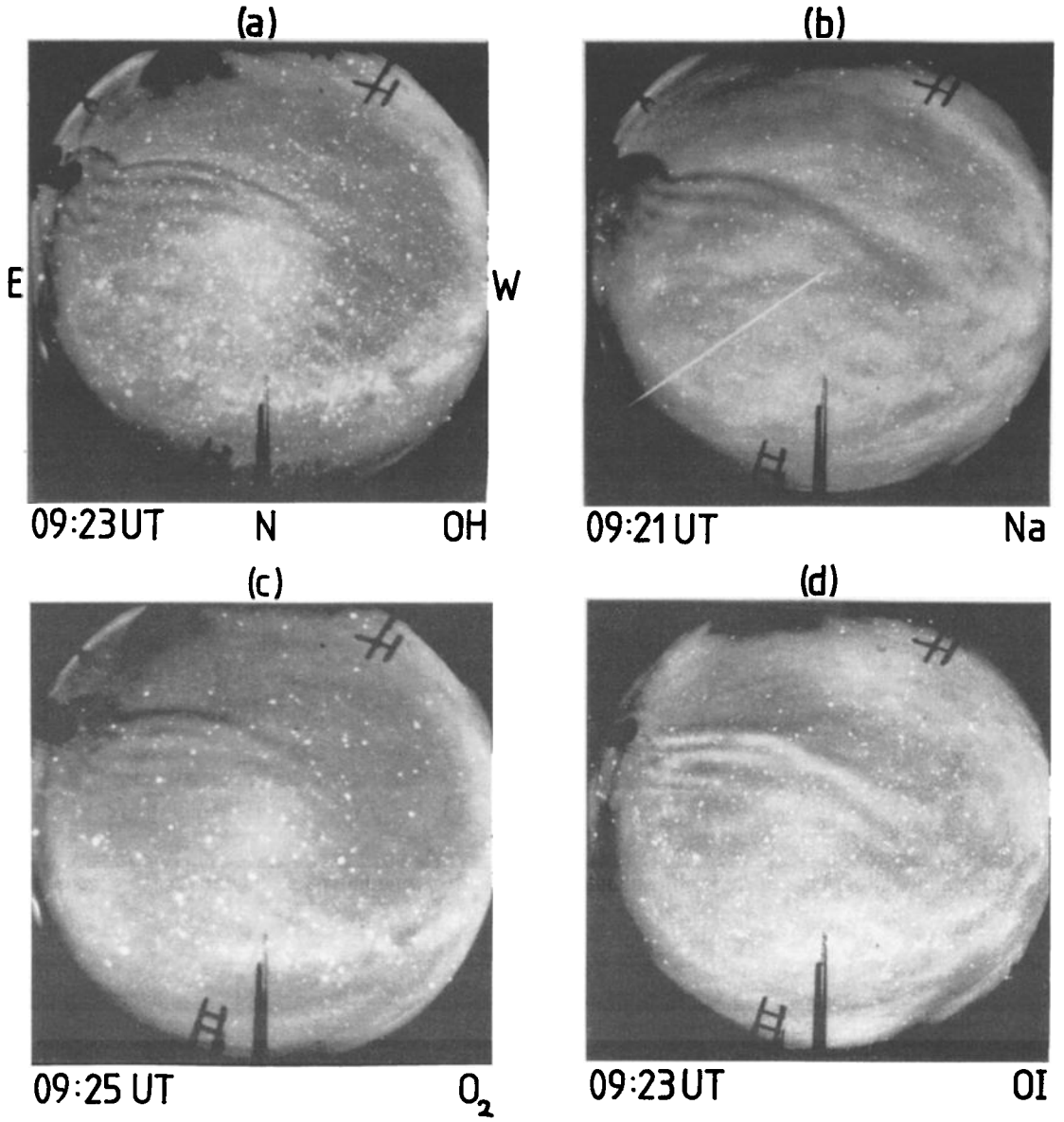

Figure 3. Event 26, as imaged by the CCD camera in the (a) OH, (b) Na, (c) O_2, and (d) OI emissions. South is to the top in the images.

times because of the finite integration time needed for each exposure (15–120 s). After correcting for this time difference using the measured horizontal phase speed, however, one can obtain approximately simultaneous maps from two (or more) different emissions. Ground maps can then be compared, and the spatial locations of several wave crests can be used to determine the magnitude of the mean phase shift between different emission layers. An alternative approach is more suitable when a single wave crest is much brighter in the images than other wave crests within the same wave pattern. In this case, the motion of the prominent waveform is followed as a function of time in two (or more) different emissions, after once again correcting for the time difference due to finite imaging time. In either case, no apparent spatial shift between the waveforms at different heights suggests that the waves are vertically evanescent or ducted, while a spatial shift between the waveforms is considered suggestive of vertical phase progression. The lack of a phase shift between images of different airglow layers is only suggestive of ducting because the phase of the intensity response of airglow depends in general on details of the airglow photochemistry, so that the exact phase relationship between the intensity and the perturbing wave depends on which airglow is being imaged.

It is important to note that this technique is most effective when the gravity waves are imaged near the zenith ($\pm 40°$). Observations at larger zenith angles can be complicated by line-of-sight effects and by difficulties in identifying and mapping accurately the geographic location of a waveform at a large range in the all-sky image format (this limitation does not adversely affect horizontal wavelength measurements which depend on a relative measure of crest separations rather than absolute positions). This analysis has been applied to several of

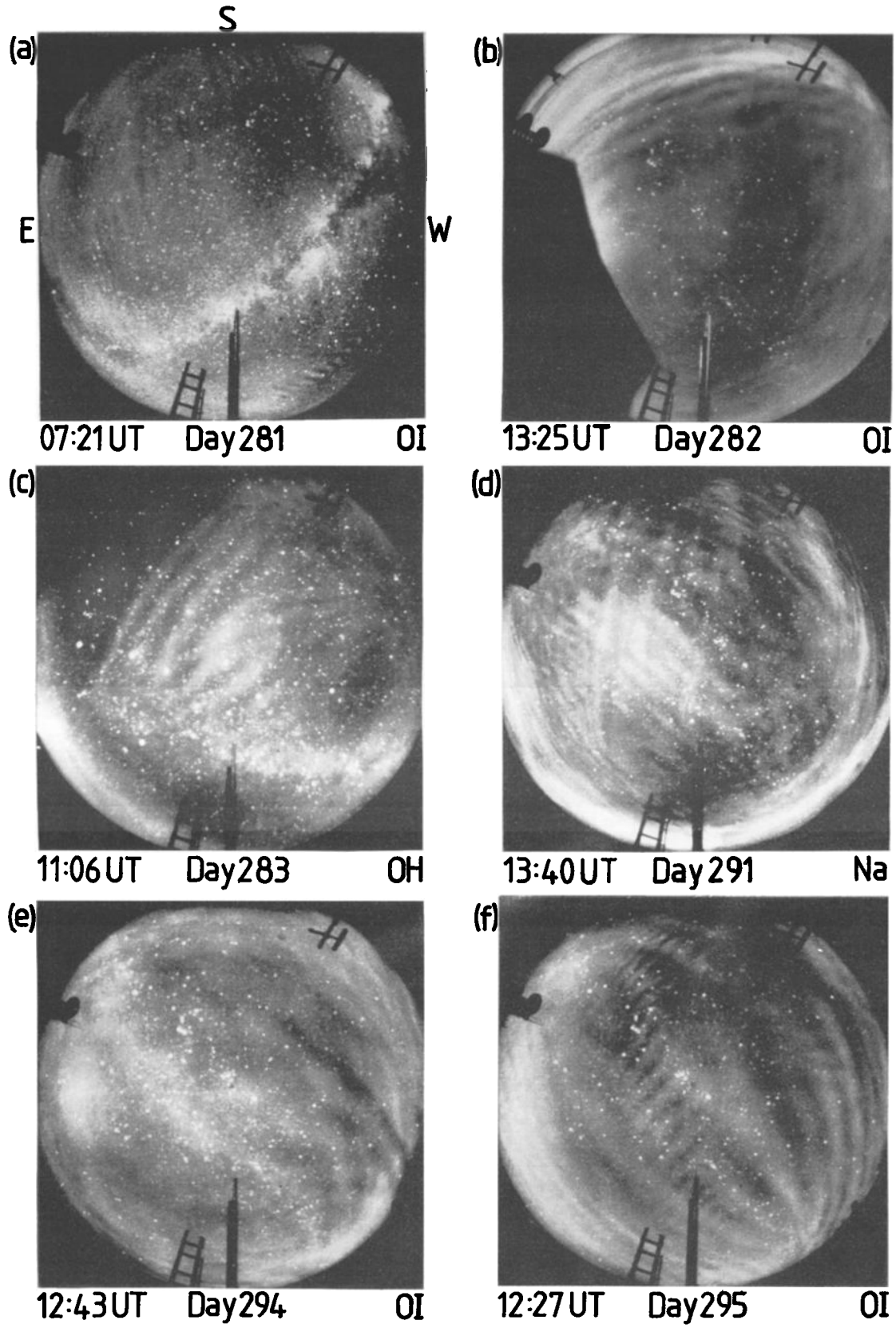

Figure 4. As in Figure 3, but for (a) event 2 imaged in the OI emission, (b) event 10 imaged in OI, (c) event 13 imaged in OH, (d) event 25 imaged in Na, (e) event 34 imaged in OI, and (f) event 36 imaged in OI.

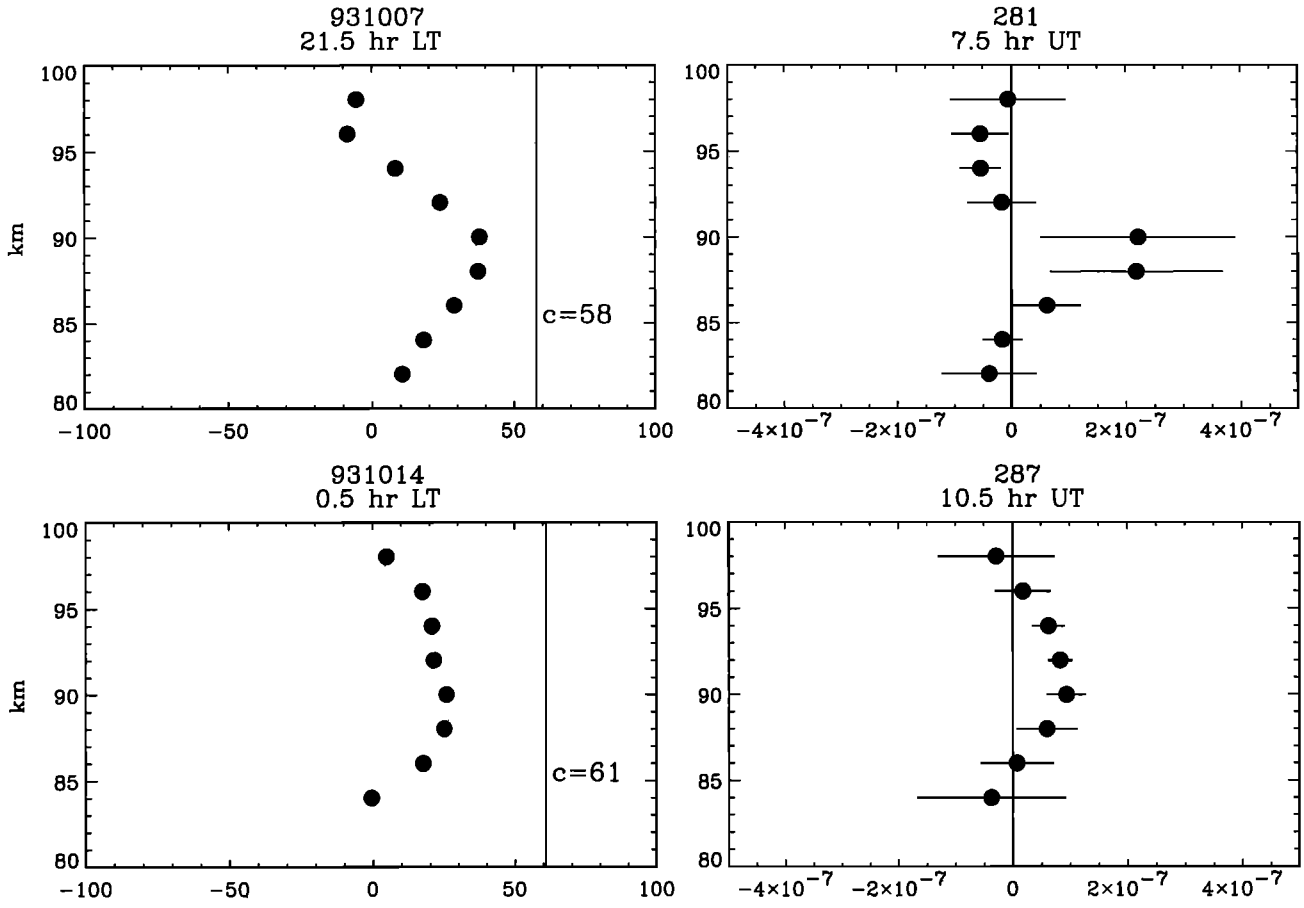

Figure 5. (left) Measured wind profiles along the direction of wave propagation for events (top) 2 and (bottom) 22, (right) together with inferred values of m^2 in each case.

the wave events listed in Table 2 (whenever possible) to investigate their nature. However, before presenting these results we first examine the characteristics of the waves as determined by the radar measurements of the prevailing mean wind field during each event.

4.2. Inferred Wave Parameters

For each wave event, 3-hour mean winds determined from the MF radar data were used to generate profiles of $\bar{u}$, the projection of the mean wind vector onto the wave azimuth. These values of $\bar{u}$ were then inserted into equation (2) together with measurements of λ_h and c to calculate profiles of m^2 in each case. In each case the error was estimated assuming mean uncertainties for c and λ_x (as determined from the image data analysis) of $\delta c/c = 0.05$ and $\delta\lambda_x/\lambda_x = 0.03$. The error in the 3-hour mean wind was determined spectrally and was found to be less than 1 m s^{-1}, consistent with error bars of 7–10 m s^{-1} for the 2-min wind data [*Fritts and Isler*, 1994]. An uncertainty in the estimated height from the radar data of ~2 km was used in determining the uncertainty in $\bar{u}_{zz}$. Some recent work suggests that during the time of this study the Hawaii radar may have somewhat underestimated winds at the uppermost heights due to receiver saturation. This implies an additional source of error at the uppermost heights which is difficult to quantify. Finally, as mentioned in section 2, we have chosen 3-hour mean winds in order to address inherent limitations to the analysis associated with the spatial separation of the imager and the radar.

The results of this analysis are summarized in Table 2. Unless $m^2 > 0$ throughout the wind profile, the λ_z column has been left empty. Since λ_z varies with $\bar{u}$, a range of λ_z is given rather than a single value for those cases where m^2 was positive everywhere.

For each event, the values for $\bar{u}$ given in Table 2 were determined as near as possible to the assumed mean altitude of the dominant nightglow emission. Intrinsic wave periods determined for these values of $\bar{u}$ were in most cases less than 10 min, providing further justification for our choice of 3-hour means to represent as closely as possible the background wind environment. Table 2 also shows the propagating or nonpropagating character over the entire height range of the wind profile. In several cases, examples were found that showed a region of positive m^2 bounded by regions where m^2 was negative, indicative of a Doppler duct. Event 2 is a particularly good example of a Doppler duct. This wave motion was detected only in the OI emission (Figure 4a) and is discussed in more detail later. Many other cases exhibited m^2 either positive or negative over the entire altitude range of the wind profile, implying that the wave was vertically propagating or evanescent, respectively. Other cases were less clear and showed a single change in sign of m^2 over the altitude range of the wind profile. In light of these possibilities, individual wave

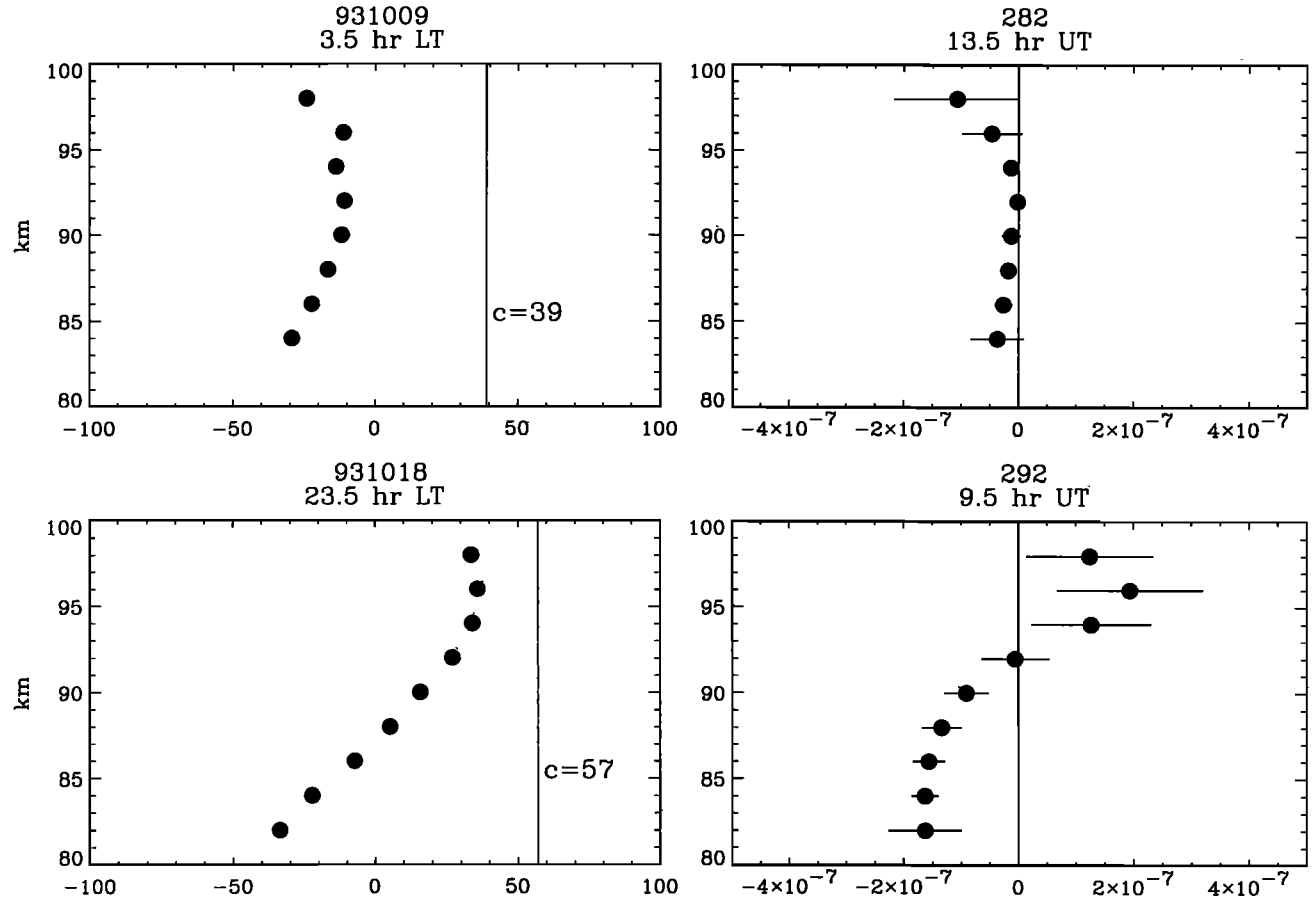

Figure 6. As in Figure 5, but for events (top) 10 and (bottom) 26.

events are characterized in Table 2 as propagating ($m^2 > 0$ everywhere), ducted (Doppler duct, with an $m^2 > 0$ region bounded by $m^2 < 0$ regions), evanescent ($m^2 < 0$ everywhere), and evanescent or ducted (a single change of sign of m^2 within the height interval). Considering the relatively narrow altitude range of the available wind profiles, it is not surprising that it is not always possible to resolve the full vertical extent of the duct. Cases categorized as "evanescent or ducted" in Table 2 may represent situations when only one edge of a Doppler duct was clearly resolved by the limited altitude range of the wind data. Similarly, the purely evanescent cases may be instances where the duct itself was beyond the altitude range of the wind data, and only an evanescent region outside the duct was resolved. Thus all of the events listed as ducted, evanescent, or both in Table 2 can be considered to be suggestive of ducted behavior. Of the total of 36 events presented here, 28 fall under ducted, evanescent, or both and only 8 occur in the freely propagating column. This indicates that a significant fraction, up to ~75% of the cases studied, were evanescent or ducted waves.

4.3. Illustrative Examples

Examples of wave events inferred to be vertically ducted or evanescent are shown in Figures 5 and 6. In each case, the left side shows the measured profile of $\bar{u}$, while the value of c for the event is indicated by a vertical line. The right sides depict the inferred profiles of m^2. Plots for events 2 and 22 are shown in Figure 5 (an image corresponding to event 2 was shown in Figure 4a). These are examples of Doppler ducts, illustrating how the wind Doppler shifts $|c - \bar{u}|$ so that a region of positive m^2 is bounded by regions of negative m^2. Note that m^2 maxima occur where $|c - \bar{u}|$ is a minimum. As mentioned before, event 2 was only detected in the OI emission and, perhaps surprisingly, was not detected in the emissions which originate closer to the wind-inferred ducted region (in this case, ~85–92 km). This sometimes occurs in other cases and could be due to a variety of reasons. First, as mentioned previously, the OI images generally had the greatest contrast, and so waves were most easily detected in them. Second, in general, there is no reason to expect to see ducted waves only in the ducted (i.e., $m^2 > 0$) region. In the evanescent region outside a Doppler duct, wave amplitudes fall off exponentially; how rapid this falloff is depends on the wind and stability profiles responsible for each duct. In some cases, such as event 2 (Figure 5), this falloff is not steep. Third, other waves and/or turbulence may be present which obscure the signature of the ducted wave at one height but not at another. For example, a wave propagating upward from below may have reached the OH layer but not the OI layer.

Plots for events 10 and 26 are shown in Figure 6 (images corresponding to these events were shown in Figures 4b and 3, respectively). Event 10 is an example of an evanescent region throughout the range of the wind profile, while event 26 is an instance where m^2 undergoes a single change in sign. In the latter case, this may represent the lower side of a Doppler duct, which may extend beyond the maximum height of the wind

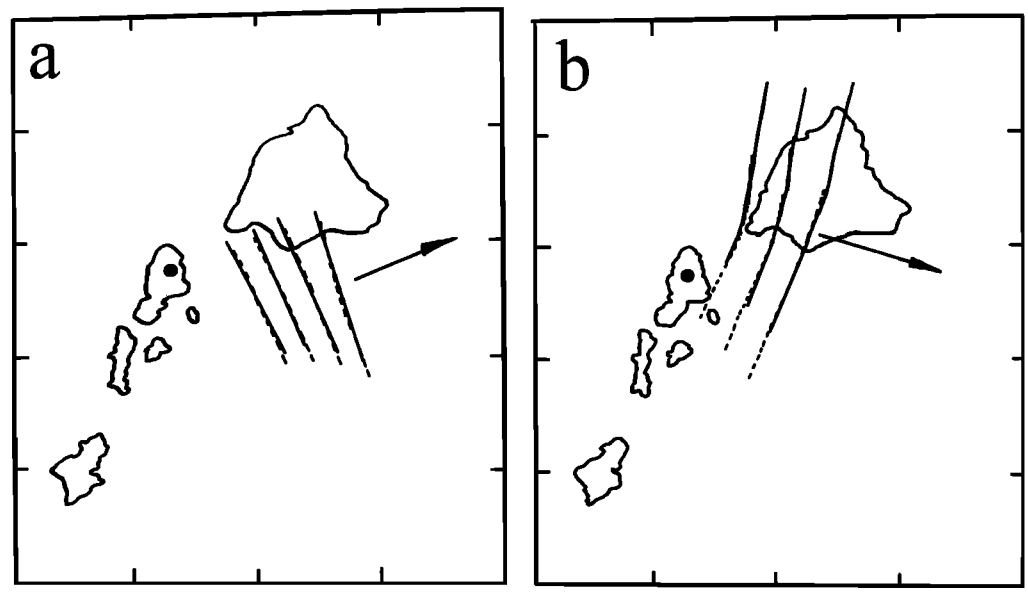

Figure 7. Superimposed maps from images of the OH emission (~87 km) and the OI emission (~96 km) corresponding to the events in Figure 6 for (a) event 10 and (b) event 26.

profile. Assuming this to be the case, then both of these events imply waves which were not freely propagating vertically.

For comparison with these inferences, superimposed maps of the OH and OI nightglow waveforms for events 10 and 26 are shown in Figure 7. These emissions were chosen as they are the farthest apart (~10 km) and therefore should be the most sensitive for detecting significant phase shifts associated with the tilt of the wave phase surfaces. As indicated earlier, it was

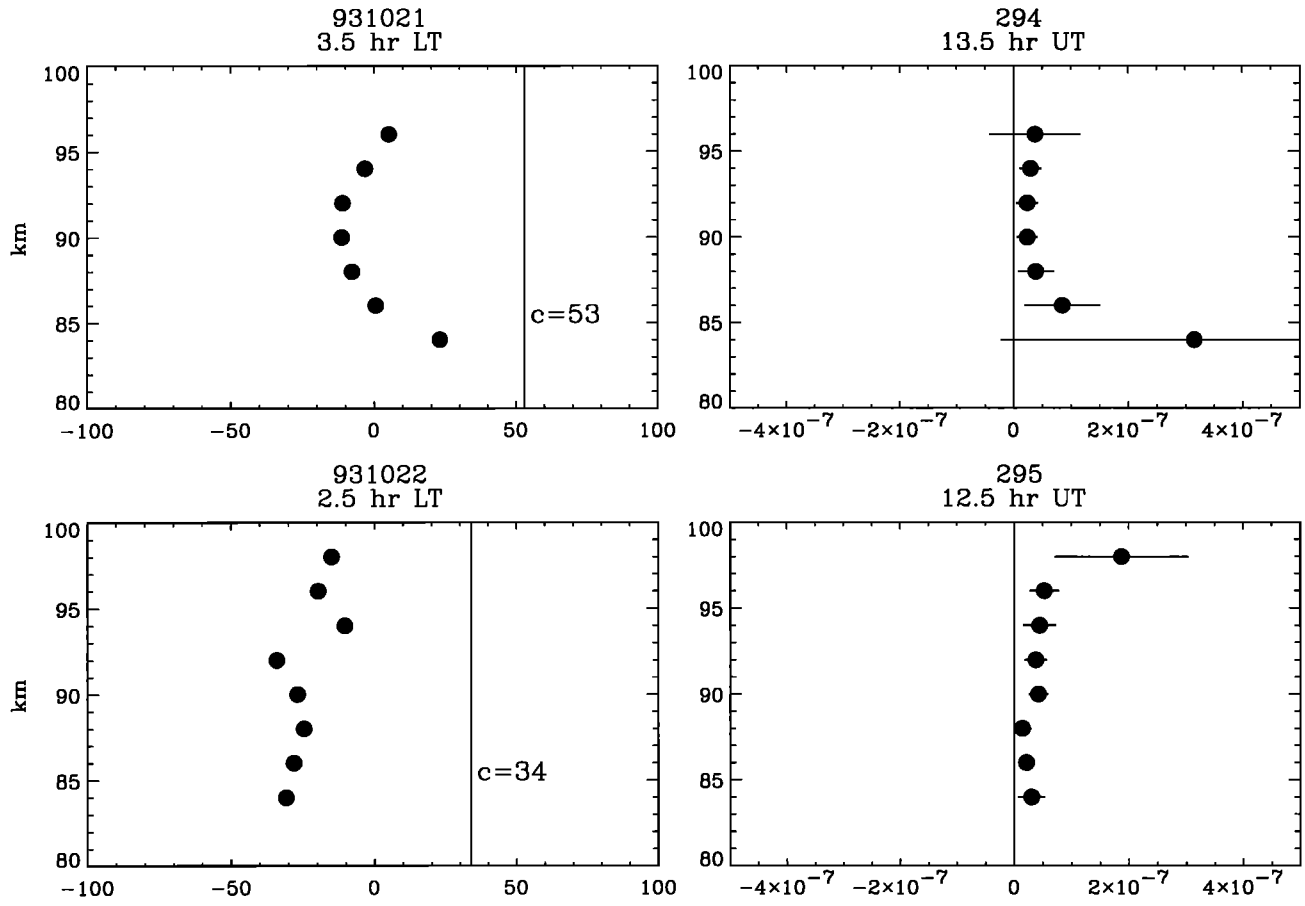

Figure 8. As in Figure 5, but for events (top) 34 and (bottom) 36.

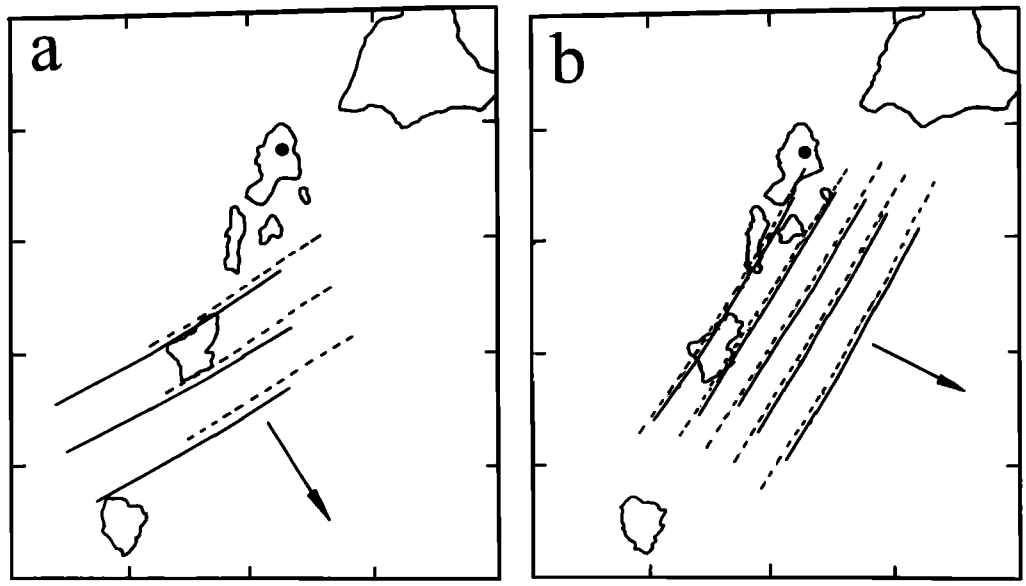

Figure 9. As in Figure 7, but corresponding to the events shown in Figure 8 for (a) event 34 and (b) event 36.

usually not possible to make such ground maps in the cases where Doppler ducts were fully resolved as the wave structure was often only detectable in one (or sometimes two close by) emissions. The map for event 10 was made using several adjacent crests in the wave train imaged at one time, while the map for event 26 was made for the prominent leading waveform and plots its motion as a function of time in the OH and OI emissions. In both cases, a single line has been drawn to mark the location of the center of each bright band measured; the OI features are depicted by the solid lines and the OH features are depicted by the dashed lines. This was done so that the lines would represent the same wave phase, independent of the width of the band, which can depend on the horizontal displacement of the wave during the differing exposure times, or on factors related to airglow photochemistry. Figure 7 shows that in both cases the phase shifts between the OH and OI wave crests are small, indicating that within the limits of the measurement accuracy these two events exhibited no vertical component of phase progression. This agrees with the nonpropagating character inferred from the radar for these events.

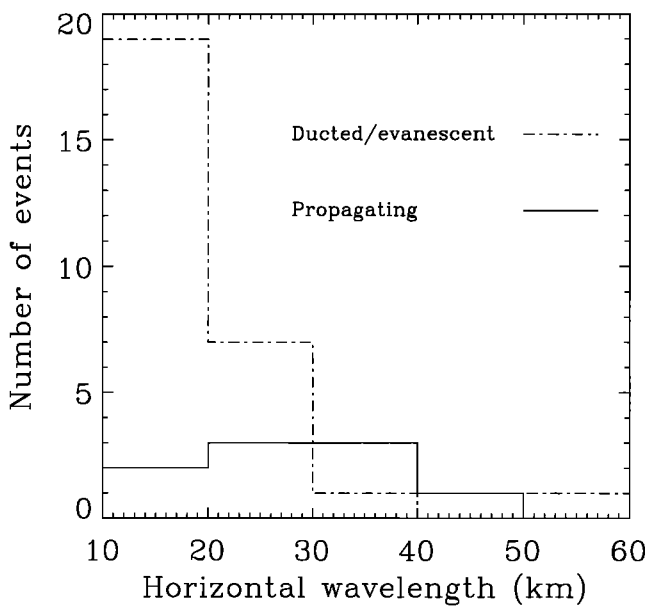

Figure 10. Histogram comparing the number of propagating waves to the number of nonpropagating waves per horizontal wavelength bin.

In contrast to the previous examples, two examples of waves (events 34 and 36) that were inferred to be vertically propagating are shown in Figure 8 (images corresponding to these events are shown in Figures 4e and 4f). In these two cases, $m^2 > 0$ throughout the height range of the wind profile. For event 34, the inferred vertical wavelength ranged from ~10 to 40 km, while for event 36 it ranged from ~15 to 55 km. Ground maps showing the locations of superimposed OH and OI wave crests for these two events are shown in Figure 9. For consistency the same format is used as in Figure 7, and once again one map illustrates the motion of a single prominent OH/OI waveform as a function of time (event 34), while the other depicts several crests at the same time in both emissions (event 36). In both maps a significant phase shift is evident between the OH and OI waveforms, in good agreement with the inferred propagation character determined from the radar data. Accurate determination of the magnitude of the phase shift from the image data depends critically on the separation of the two emission layers, which was not measured during this campaign. However, a larger phase shift was determined for event 34 than for event 36, which is consistent with the shorter vertical wavelength for event 34 relative to that for event 36 deduced from the radar data comparison.

4.4. Scale Dependence

To summarize the measurements and results presented in Table 2, a histogram plot of all 36 events is given in Figure 10, where the number of events of each type have been binned by horizontal wavelength. Events classified in the last three columns of Table 2 are considered to be nonpropagating in Figure

10; a similar histogram plot is shown for the waves which were inferred to be freely propagating. As can be seen, there is an overall tendency for ducted or evanescent behavior to occur more frequently for waves which have smaller horizontal scales. This result is consistent with Doppler ducting theory as small-scale waves have larger horizontal wavenumbers (k in equation (2)) and thus more easily encounter variations in $c - \bar{u}$ leading to $m^2 < 0$.

5. Potential Wave Sources

One impact of this study is the investigation of potential wave sources. In the absence of ducting, short-period waves generated in the troposphere would be expected to propagate relatively short horizontal distances (typically a few hundred kilometers) from the source region before penetrating into the upper mesosphere. This is because the elevation angle at which the gravity wave energy is directed depends on the wave period, and short-period waves tend to propagate much more steeply than longer-period waves. For source studies, a first estimate of the horizontal range of propagation can be estimated from the dispersion relation. However, background winds in the intervening stratosphere and lower mesosphere can act either to impede the upward motion of these waves by absorption at critical levels or to extend their horizontal range of propagation by Doppler shifting their motions to longer intrinsic periods. Similarly, ducting in the mesosphere and lower thermosphere can significantly increase the distance over which waves can progress horizontally before dissipating or penetrating to higher altitudes.

For waves observed at mesopause altitudes, investigations of their sources are notoriously difficult for the above reasons and only on rare occasions have isolated sources been positively identified [e.g., *Taylor and Hapgood*, 1988]. One source that is thought to be important for generating extensive wave motions are tropospheric fronts. On numerous occasions during the ALOHA-93 campaign (March–April 1990) extensive, short-period waves were observed to progress towards the SE [*Taylor and Hill*, 1991]. An initial investigation of the sources of these events revealed a series of frontal systems progressing toward the Hawaiian Islands from the NW. However, they were all at a significantly larger range than would be expected assuming the waves were freely propagating in nature, suggesting either wave ducting was occurring or other sources were responsible for their generation [*Taylor and Edwards*, 1991]. More recently, during the ALOHA-93 campaign one of the primary flights of the airborne instrumentation was toward a "storm front" to investigate wave generation by such systems. The airborne all-sky imager recorded considerable wave activity as the aircraft approached within a few hundred kilometers to the NW of Maui [*Swenson and Espy*, 1995]. Wave motions exhibiting a similar horizontal phase speed (39 m s^{-1}) and orientation (150°) were recorded several hours later by our all-sky imager located on Haleakala [*Taylor et al.*, 1995a]. An example image of this wave pattern in the OI emission was given in Figure 4b (event 10) which shows the waves as they appeared at low elevations toward the SE sometime after passing through the zenith. Of considerable interest here is the fact that this particular wave pattern was determined to be evanescent using the MF wind data. Thus it appears that Doppler ducting played a major role in extending the horizontal range over which the wave was able to propagate on this occasion.

The similarity of this wave motion to those observed frequently during the ALOHA-93 campaign suggests that these disturbances may also have been signatures of Doppler ducted waves. Assuming this to be so leads us to speculate that Doppler ducting may well be commonplace. This result may also help account for the relatively high occurrence frequency of wave structure that has now been observed during both ALOHA campaigns in the absence of major orographic forcing or nearby tropospheric disturbances such as storm fronts and jet streams [*Taylor and Hill*, 1991; *Swenson and Espy*, 1995; *Taylor et al.*, 1995a].

6. Summary and Conclusions

Simultaneous MF radar and high-resolution imaging measurements were made from two low-latitude, oceanic sites located on the islands of Kauai and Maui shortly after the fall equinox (October 6–23) 1993 during the ALOHA-93 campaign. A study of 36 discrete quasi-monochromatic wave events has revealed a significant fraction of them to be occurrences of wave ducting, with ducted or evanescent behavior inferred for up to ~75% of the wave events. Independent evidence for ducted or evanescent versus propagating behavior was obtained using measurements of the same wave structures in different nightglow emissions spanning ~80–100 km. In each instance, where accurate ground maps from the different emissions could be compared, there was good accord between the observed propagating character of the waves and the propagating character inferred from the radar wind data. Furthermore, smaller-scale waves were found more likely to be ducted than larger-scale waves, in agreement with Doppler ducting theory which predicts that smaller-scale waves are more likely to be ducted than larger-scale waves because k^2 is large.

Owing to natural limitations of the imaging technique, only waves with horizontal scales less than ~250 km and vertical scales greater than ~8–10 km could be studied. Waves at these scales tend to have short periods; whether our finding of ducted behavior in up to ~75% of the cases is representative of short-period wave behavior for other geographical regions (e.g., mountainous sites) and/or other times of the year is an important question that has yet to be addressed. However, the predominance of ducted waves over vertically propagating waves revealed by this study has important implications for future observational and/or modeling studies which assume small-scale waves to be vertically propagating, since their transports of energy and momentum may occur over a much larger geographic area than would normally be achieved by vertical propagation.

Acknowledgments. Support for the optical measurements was provided by the NSF/CEDAR program under grant ATM 93024844 and by the Air Force Office of Scientific Research (AFOSR) Geophysics Directorate, under contract F19628-93-C-0165, as part of the SOAR program. Support for the radar measurements as part of the CADRE campaign and support for airglow modeling was provided by NSF under grants ATM93-02050, ATM93-01981, and ATM94-14177 and by AFOSR under contract F49620-96-1-0300. We acknowledge the assistance of J. Albetski, Thermotrex Corporation, for arranging our use of the DOE facility, Haleakala Crater, Maui, for the optical measurements. We also thank V. Taylor for assistance with the image measurements and M. Bishop and S. Clarke for their help with the data analysis.

References

Baker, D. J., Jr., and A. T. Stair, Rocket measurements of the altitude distributions of the hydroxyl airglow, *Phys. Scr.*, *37*, 611–622, 1988.

Chimonas, G., and C. O. Hines, Doppler ducting of atmospheric gravity waves, *J. Geophys. Res.*, *91*, 1219–1230, 1986.

Francis, S. H., Global propagation of atmospheric gravity waves: A review, *J. Atmos. Terr. Phys.*, *37*, 1011–1054, 1974.

Fritts, D. C., Gravity wave saturation in the middle atmosphere: A review of theory and observations, *Rev. Geophys.*, *2*, 275–307, 1984.

Fritts, D. C., A review of gravity wave saturation processes, effects, and variability in the middle atmosphere, *Pure Appl. Geophys.*, *130*, 343–371, 1989.

Fritts, D. C., and J. R. Isler, Mean motions and tidal and two-day structure and variability in the mesosphere and lower thermosphere over Hawaii, *J. Atmos. Sci.*, *51*, 2145–2164, 1994.

Fritts, D. C., and L. Yuan, An analysis of gravity wave ducting in the atmosphere: Eckart's resonances in thermal and Doppler ducts, *J. Geophys. Res.*, *94*, 18,455–18,466, 1989.

Greer, R. G. H., and G. T. Best, A rocket-borne photometric investigation of the oxygen lines at 5577-A and 6300-A, the sodium D-lines and continuum at 5300-A in the night airglow, *Planet. Space Sci.*, *15*, 1857–1866, 1967.

Hapgood, M. A., and M. J. Taylor, Analysis of airglow image data, *Ann. Geophys.*, *38*, 805–813, 1982.

Hecht, J. H., R. L. Walterscheid, and M. N. Ross, First measurements of the two-dimensional horizontal wave number spectrum from CCD images of the nightglow, *J. Geophys. Res.*, *99*, 11,449–11,460, 1994.

Hines, C. O., Internal gravity waves at ionospheric heights, *Can. J. Phys.*, *38*, 1441–1481, 1960.

Offermann, D., and A. Drescher, Atomic oxygen densities in the lower thermosphere as derived from in situ 5577-A night airglow and mass spectrometer measurements, *J. Geophys. Res.*, *78*, 6690–6702, 1973.

Smith, S. A., D. C. Fritts, and T. E. VanZandt, Evidence for a saturated spectrum of atmospheric gravity waves, *J. Atmos. Sci.*, *44*, 1404–1410, 1987.

Swenson, G. R., and P. J. Espy, Observations of 2-dimensional airglow structure and Na density from the ALOHA, October 9, 1993 'storm flight,' *Geophys. Res. Lett.*, *22*, 2845–2848, 1995.

Swenson, G. R., M. J. Taylor, P. J. Espy, C. Garndner, and X. Tao, ALOHA-93 measurements of intrinsic AGW characteristics using airborne airglow imager and groundbased Na wind temperature lidar, *Geophys. Res. Lett.*, *22*, 2841–2844, 1995.

Taylor, M. J., and R. Edwards, Observations of short-period mesospheric wave patterns: In situ or tropospheric wave generation?, *Geophys. Res. Lett.*, *18*, 1337–1340, 1991.

Taylor, M. J., M. B. Bishop, and V. Taylor, All-sky measurements of short-period waves imaged in the OI (557.7 nm), and Na (589.2 nm) and near infrared OH and $O_2(0, 1)$ nightglow emissions during the ALOHA-93 campaign, *Geophys. Res. Lett.*, *22*, 2833–2836, 1995a.

Taylor, M. J., D. C. Fritts, and J. R. Isler, Determination of horizontal and vertical structure of an unusual pattern of short period gravity waves imaged during ALOHA-93, *Geophys. Res. Lett.*, *22*, 2837–2840, 1995b.

Taylor, M. J., Y. Y. Gu, X. Tao, C. S. Gardner, and M. B. Bishop, An investigation of intrinsic gravity wave signatures using coordinated lidar and nightglow image measurements, *Geophys. Res. Lett.*, *22*, 2853–2856, 1995c.

Taylor, M. J., and M. A. Hapgood, Identification of a thunderstorm as a source of short period gravity waves in the upper atmospheric nightglow emissions, *Planet. Space Sci.*, *36*, 975–985, 1988.

Taylor, M. J., and M. A. Hapgood, On the origin of ripple-type wave structure in the OH nightglow emission, *Planet. Space Sci.*, *38*, 1421–1430, 1990.

Taylor, M. J., M. A. Hapgood, and P. Rothwell, Observations of gravity wave propagation in the OI (557.7 nm), Na (589.2 nm) and the near infrared OH nightglow emissions, *Planet. Space Sci.*, *35*, 413–427, 1987.

Taylor, M. J., and M. J. Hill, Near infrared imaging of hydroxyl wave structure over an ocean site at low latitudes, *Geophys. Res. Lett.*, *18*, 1333–1336, 1991.

Taylor, M. J., G. R. Swenson, and V. Taylor, Height measurements of OI (557.7 nm) gravity wave structure over the Hawaiian Islands during ALOHA-93, *Geophys. Res. Lett.*, *22*, 2881–2884, 1995d.

Tuan, T. F., and D. Tadic, A dispersion formula for analyzing 'model interference' among guided and free gravity wave modes and other phenomena in a realistic atmosphere, *J. Geophys. Res.*, *87*, 1648–1668, 1982.

Wang, D. Y., and T. F. Tuan, Brunt-Doppler ducting of small-period gravity waves, *J. Geophys. Res.*, *93*, 9916–9926, 1988.

D. C. Fritts, Colorado Research Associates, 3380 Mitchell Lane, Boulder, CO 80301.

J. R. Isler, Physics Department, Wagner College, Staten Island, NY 10301.

M. J. Taylor, Space Dynamics Laboratory, Utah State University, Logan, UT 84322.

(Received June 5, 1996; revised June 18, 1997;
accepted June 18, 1997.)